

# Variational LOCC-assisted quantum circuits for long-range entangled states

Yuxuan Yan,<sup>1,\*</sup> Muzhou Ma,<sup>2,\*</sup> You Zhou,<sup>3,†</sup> and Xiongfeng Ma<sup>1,‡</sup>

<sup>1</sup>*Center for Quantum Information, Institute for Interdisciplinary Information Sciences, Tsinghua University, Beijing 100084, China*

<sup>2</sup>*Department of Electronic Engineering, Tsinghua University, Beijing 100084, China*

<sup>3</sup>*Key Laboratory for Information Science of Electromagnetic Waves (Ministry of Education), Fudan University, Shanghai 200433, China*

Long-range entanglement is an important quantum resource, especially for topological orders and quantum error correction. In reality, preparing long-range entangled states requires a deep unitary circuit, which poses significant experimental challenges. A promising avenue is offered by replacing some quantum resources with local operations and classical communication (LOCC). With these classical components, one can communicate information from mid-circuit measurements in distant parts of the system, which results in a substantial reduction of circuit depth in many important cases. However, to prepare general long-range entangled states, finding LOCC-assisted circuits of a short depth remains an open question. Here, we address such a challenge by proposing a quantum-classical hybrid algorithm to find ground states of given Hamiltonians based on parameterized LOCC protocols. We introduce an efficient protocol for estimating parameter gradients and use such gradients for variational optimization. Theoretically, we establish the conditions for the absence of barren plateaus, ensuring trainability at a large system size. Numerically, the algorithm accurately solves the ground state of long-range entangled models, such as the perturbed GHZ state and surface code. Our results clearly demonstrate the practical advantage of our algorithm in the accuracy of estimated ground state energy over conventional unitary variational circuits, as well as the theoretical advantage in creating long-range entanglement.

## I. INTRODUCTION

Long-range entanglement structures play an essential role in many quantum information processing scenarios, which are defined by the minimal circuit depth required for their preparation. Specifically, long-range entangled states require deep unitary circuits to be prepared from a product state; asymptotically, the depth requirement would be unbounded in the large system limit [1, 2]. A typical example of long-range entangled states is the Greenberger–Horne–Zeilinger (GHZ) state, which finds important applications in quantum communication, cryptography, and computation. In addition, as a canonical example exhibiting topological orders, the surface code state is also long-range entangled and consequently serves as a resource for topological quantum memory and computation [3, 4]. More generally, quantum topological order and error-correcting codes essentially rely on long-range entanglement [5].

Important as they are, the preparation of long-range entangled states is severely challenged by their depth requirements [6–8]. Fortunately, a promising solution is found by introducing local operations and classical communication (LOCC). With the assistance of LOCC, circuits would include mid-circuit measurements and feed-forwards, where measurement results determine the subsequent quantum local operations. Note that LOCC-assisted circuits are also referred to by other terminolo-

gies, including circuits with mid-circuit measurements, adaptive circuits, and dynamic circuits. The essential role of LOCC in these circuits is to communicate information among distant subsystems and thereby create long-range correlations, which necessitates a significantly larger depth for circuits with only local unitary gates [9]. The introduction of LOCC brings great success in preparing surface code states in a constant depth [10–12], and it was later extended to other topologically ordered systems [13–17] and other important states in quantum information processing, such as the GHZ state [12, 18], W states [12, 19, 20], and Dicke states [19]. Recently, progress has also been made in preparing tensor-network states [21–25]. These findings provide theoretical insights into the power of LOCC-assisted circuits in terms of depth reduction.

Despite the successes of previous important cases, the full potential of LOCC in general state preparation is largely unexplored. A systematic approach is still needed to find short-depth LOCC-assisted circuits for preparing general states, especially long-range entangled ones. In essence, this requires optimization over various LOCC-assisted circuits. Such an optimization task exists for scenarios without LOCC assistance and is often solved by variational quantum algorithms [26–32]. However, extending the variational toolkits to the LOCC case remains unexplored and challenging. It is unclear whether previous techniques, especially the quantum gradient protocol, are compatible with LOCC. Furthermore, the number of parameters that define complex LOCC protocols is large in general, which would induce computational inefficiency. Note that a naive approach may even introduce exponentially many parameters. More impor-

\* These authors contributed equally to this work.

† [you.zhou@fudan.edu.cn](mailto:you.zhou@fudan.edu.cn)

‡ [xma@tsinghua.edu.cn](mailto:xma@tsinghua.edu.cn)

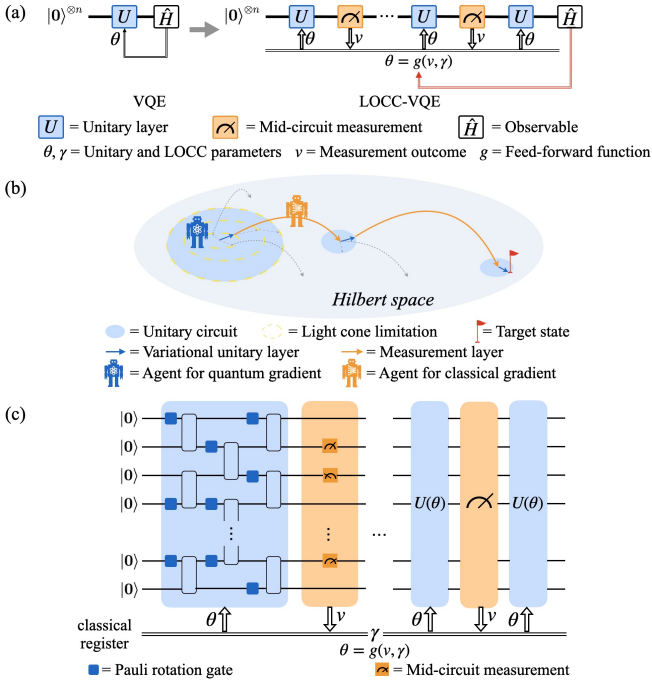


FIG. 1: LOCC-VQE scheme. Blue blocks represent unitary circuits, and orange blocks represent mid-circuit measurements. (a) Algorithm structure of LOCC-VQE. Gradient information is obtained for optimizing the LOCC parameters  $\gamma$  in the feedback loop, represented by the red arrow. This feedback loop is the main difference compared to variational quantum algorithms. (b) Exploring the Hilbert space with LOCC-VQE. Among all possible paths, represented by dash arrows, agents obtained the gradient information to find an optimized state preparation path, represented by solid arrows, to reach the target state. LOCC enables states to jump in the Hilbert space, breaking the light cone limitation on unitary circuits, as illustrated by the dotted yellow circles. (c) Variational LOCC-assisted quantum circuits. Parameterized unitary layers, represented in blue, and mid-circuit measurement layers, represented in orange, are applied alternatively.

tantly, the trainability of variational LOCC-assisted circuits is a crucial open problem. For variational algorithms, barren plateaus, i.e., the gradients vanishing exponentially as the system size scales up, are frequently encountered challenges. Barren plateaus would often arise with the increase in circuit depth and the number of parameters [33], which becomes even more severe when considering physical noise accumulation. The introduction of LOCC's assistance may ease the depth problem but would also worsen barren plateaus without a proper design.

In this work, we tackle these challenges by proposing the LOCC-assisted variational quantum eigensolver (LOCC-VQE) to solve the ground state of a given Hamiltonian, as depicted in Fig. 1. To figure out the opti-

mal LOCC protocol, we propose an efficient quantum-classical hybrid approach to estimate parameter gradients and present explicit and reasonable conditions for the absence of barren plateaus. Based on these gradients, we can perform gradient-based optimization to minimize the energy and solve the ground state problem via LOCC-VQE, as depicted in Fig. 1(a). Notably, LOCC protocols can be selected with flexibility, allowing the incorporation of classical computations in various forms, such as look-up tables or neural networks. By choosing appropriate protocols, we offer efficient and flexible parameterization that provides LOCC-assisted advantages while ensuring trainability by avoiding barren plateaus, as depicted in Fig. 1 (b).

## II. VARIATIONAL LOCC-ASSISTED QUANTUM CIRCUITS

We consider the following general parameterization: Each unitary gate layer encompasses Pauli rotation gates with variational parameters  $\theta$ , as depicted in Fig. 1 (c). These gate parameters are determined by classical protocol with measurement outcomes denoted by  $\mathbf{v}$ . The classical protocol is a function  $g$  with LOCC parameters  $\gamma$ , by which gate parameters are computed as  $\theta = g(\gamma, \mathbf{v})$ . Note that our parameterization does not assume any specific circuit architecture or structures of LOCC protocols.

Since LOCC parameters  $\gamma$  are independent variables that define the circuit, we will denote the output state as  $\Psi_\gamma$ . The state can be considered the mixture of post-selected states with different mid-circuit measurement outcomes,

$$\Psi_\gamma = \sum_{\mathbf{v}} P_\theta(\mathbf{v}) \Phi_{\theta, \mathbf{v}}, \quad (1)$$

where  $P_\theta(\mathbf{v})$  is the probability of measurement outcome  $\mathbf{v}$  and  $\Phi_{\theta, \mathbf{v}}$  is the post-measurement state.

Our goal is to find the optimal  $\gamma$  that minimizes the energy of a given Hamiltonian  $\hat{H}$ , i.e.,  $\text{Tr}[\hat{H}\Psi_\gamma]$ . Note that when optimized to a good LOCC protocol, different  $\Phi_{\theta, \mathbf{v}}$  corresponding to different mid-circuit measurement outcomes will be converted to the same pure ground state of the Hamiltonian  $\hat{H}$ .

To apply efficient gradient-based optimization, we will need the gradients  $\nabla_\gamma \text{Tr}[\hat{H}\Psi_\gamma]$ . The following proposition expresses these gradients, for which we propose an efficient quantum-classical hybrid approach.

**Proposition 1.** *The gradients of a variational LOCC-assisted circuit can be obtained as the inner product of two matrices,*

$$\frac{\partial \text{Tr}[\hat{H}\Psi_\gamma]}{\partial \gamma_k} = \text{Tr}[(\mathbf{G}^{C_k})^T \mathbf{G}^{Q_k}]. \quad (2)$$

Here, the two matrices correspond to the quantum gradient,

$$\mathbf{G}^{Q_k} = \left\{ \mathbf{g}_{i,j}^{Q_k} \right\} = \left\{ \frac{\partial \text{Tr} \left[ \hat{H} P_{\theta}(\mathbf{v}_i) \Phi_{\theta, \mathbf{v}_i} \right]}{\partial \theta_j} \Big|_{\theta_j = g_j(\gamma, \mathbf{v}_i)} \right\} \quad (3)$$

and classical gradients,

$$\mathbf{G}^{C_k} = \left\{ \mathbf{g}_{i,j}^{C_k} \right\} = \left\{ \frac{\partial g_j(\gamma, \mathbf{v}_i)}{\partial \gamma_k} \right\} \quad (4)$$

respectively, where  $\mathbf{v}_i$  are measurement outcomes,  $\theta_j$  are Pauli gate rotation angles in the circuit.

This proposition implies the gradient is a combination of quantum and classical parts. Based on this proposition, we propose a protocol to estimate the gradient in Eq. (2). For estimation of the quantum part,  $\mathbf{G}^{Q_k}$ , we run shifted LOCC protocols  $g_{i\pm}(\gamma, \mathbf{v}) = g(\gamma, \mathbf{v}) \pm \frac{\pi}{2} \mathbf{e}_i$  and taking the energy difference between  $g_{i+}$  and  $g_{i-}$ . This subroutine is inspired by parameter shift rules [26–28], which directly hold for a single post-selected state  $\Phi_{\theta, \mathbf{v}_i}$ . In our protocol, we further show that post-selection can be avoided by introducing classical post-processing.

The whole gradient estimation protocol is a quantum-classical hybrid and comprised of three stages: First, for each  $\theta_i$  and corresponding shifted protocols  $g_{i\pm}$ , we estimate the contribution to the energy from different mid-circuit measurement outcomes  $\mathbf{v}$  on a quantum computer. Second, for each  $\theta_i$ ,  $\gamma_j$ , and sample  $\mathbf{v}$  from the first step, we calculate  $\frac{\partial g_i(\gamma, \mathbf{v})}{\partial \gamma_j}$  on a classical computer. Third, reweight contribution from different outcome  $\mathbf{v}$  by  $\frac{\partial g_i(\gamma, \mathbf{v})}{\partial \gamma_j}$  on a classical computer.

Compared to variational algorithms without LOCC, the second and third classical processing steps are unique to our algorithm as they combine the quantum gradients with our added LOCC components. Note that such an addition does not increase sampling overhead. Because our algorithm reuses sample data among different LOCC parameters  $\gamma_k$ , the sample complexity is only related to the number of tunable Pauli rotations in the circuit, which is the same for variational unitary circuits. Based on this gradient estimation algorithm, we can solve ground states via the workflow illustrated in Fig. 1 (a). The details of the algorithm are available in Appendix B.

### III. CONDITIONS FOR THE NON-VANISHING GRADIENTS IN LOCC-VQE

With LOCC-VQE, it is possible to prepare long-range entangled states with a low circuit depth. Such low depths appear promising for avoiding barren plateaus. However, we still need to be cautious about how the additional LOCC components impact trainability. Here, we establish the following conditions under which gradients are non-vanishing, thereby ensuring trainability.

**Theorem 1** (Conditions for non-vanishing gradients). *The following conditions can ensure the gradients do not vanish as the number of qubits scales in variational LOCC-assisted circuits:*

- A1.** *Hamiltonian is local.—The observable  $\hat{H}$  is the sum of terms whose support has a constant size.*
- A2.** *The circuit depth is constant.*
- A3.** *The gradient of the function  $g$  will not exponentially decay as the size of its input increases.*
- A4.** *Each LOCC protocol parameter  $\gamma_j$  controls a constant number of quantum gates.—The function  $g$  has a constant support regarding each  $\gamma_j$ .*
- A5.** *Each quantum gate parameter  $\theta$  is controlled by a constant number of mid-circuit measurement results.*

*Proof sketch*— The gradient of a LOCC parameter in Eq. (2) is the inner product of two vectorized high-dimensional matrices,  $\mathbf{G}^{Q_k}$  and  $\mathbf{G}^{C_k}$ . We first need to ensure these two matrices do not vanish individually. For  $\mathbf{G}^{Q_k}$  not to vanish, we acquire conditions **A1** and **A2**. These conditions can be understood from the perspective of an information propagation light cone, where information can only spread linearly in a geometrically local unitary circuit. Note that these conditions are also necessary to prevent the quantum gradient from vanishing exponentially in a unitary variational circuit, which is a special case of LOCC-assisted circuits. Similarly, we introduce condition **A3** to prevent the vanishing of classical gradients  $\mathbf{G}^{C_k}$ .

It is important to note that the non-vanishing of individual components does not guarantee the non-vanishing of the inner product. In fact, without specific conditions, such an inner product will typically vanish due to the cancellations among degrees of freedom. To address this, we introduce conditions on LOCC protocol as reflected in conditions **A4** and **A5**. These conditions imply a sparsity structure in  $\mathbf{G}^{C_k}$ . By combining this with the sparsity in  $\mathbf{G}^{Q_k}$ , we can ensure that only a constant degree of freedom contributes to the inner product, preventing the gradients from decaying as the number of qubits  $n$  in the asymptotic limit. The details of the proof are shown in Appendix C.

It is worth noting that the results of Theorem 1 are stronger than ensuring the absence of barren plateaus, which only excludes exponential vanishing but still allows for vanishing to some extent. Compared to previous findings on the absence of barren plateaus in noiseless circuits that generate long-range entanglement [34], our approach also overcomes noise-induced ones. In real experiments, the noise will unavoidably ruin information [6, 8] and induce barren plateaus for deep circuits [35]. Therefore, our algorithm is well-suited for exploring long-ranged entangled states on a large scale, even in noisy environments.

## IV. NUMERICAL RESULTS

Our numerical results are based on the current state-of-the-art tensor-network-based circuit simulator [36], with codes available in GitHub [37].

### A. One-dimensional chain models

We numerically test LOCC-VQE by solving the ground state of the Hamiltonian of the Greenberger–Horne–Zeilinger (GHZ) state with perturbations. The GHZ state is a long-range entangled state, and its parent Hamiltonian can be chosen as a one-dimensional (1D) Ising model, depicted in Fig. 2 (a),  $\hat{H}_{\text{Ising}} = -\sum_{\langle i,j \rangle} Z_i Z_j$ , where  $\langle i,j \rangle$  represent the near-neighbor sites. The problem with the Ising model is its ground state degeneracy. The ground state subspace of the Ising model contains product states, which are trivially short-range entangled. To break this degeneracy and make the GHZ state the unique ground state, a term of  $n$ -qubit tensor product of  $X$  operator is introduced,  $-h \bigotimes_i X_i$ , where  $h$  denotes the energy gap created above the GHZ state as the unique ground state. To exhibit the robustness of LOCC-VQE, we add perturbations in terms of Pauli operators on each site, resulting in

$$\hat{H}_{\text{GHZ}} = -(1-\lambda) \sum_{\langle i,j \rangle} Z_i Z_j - (h-\lambda) \bigotimes_i X_i - \lambda \sum_i P_i, \quad (5)$$

where  $\lambda$  is the perturbation strength and  $P_i \in X_i, Y_i, Z_i$  on the  $i$ -th site. Here, we use the same Pauli operators to perturb all qubits, physically representing the direction of an external uniform field.

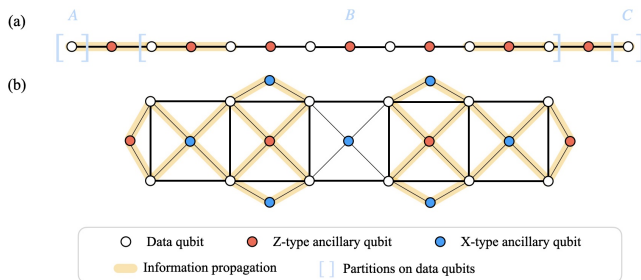


FIG. 2: Layout of qubits for (a) the parent Hamiltonian of the GHZ state and (b) the surface code. Ancillary qubits are introduced to perform multi-qubit Pauli measurements on  $X$  and  $Z$  basis, respectively. Light-blue regions  $A$ ,  $B$ , and  $C$  form a partition of the data qubits. The yellow region represents the light cone of information propagation through local two-qubit unitary gates.

In our numerical tests, we simulate an 8-qubit model, set  $h = 16$ , and test various values of perturbation strength,  $\lambda$ . We first test the energy achieved by LOCC-VQE and unitary VQE of the same depth of two with

the perturbed Hamiltonian introduced above. For variational training, we set the same number of iterations. With variational LOCC-assisted circuit ansatz, information can propagate beyond the light cone limitation placed on unitary circuit ansatz, making it possible for long-range entanglement to emerge within shallow depth. The circuit design is inspired by the LOCC protocol for preparing a non-perturbed GHZ state as illustrated in [12]. We parameterized near-neighbour data qubits coupled to an ancilla qubit and measured them, and the measurement outcomes were fed into the classical function. Detailed circuit parameterization methods are described in Appendix E.

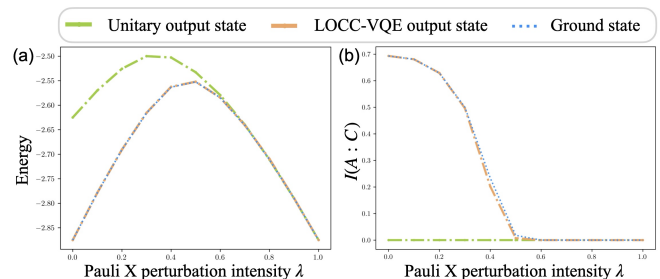


FIG. 3: Numerical simulation results of solving the parent Hamiltonian of the 8-qubit GHZ state with Pauli  $X$  perturbations with depth two circuits. (a) Comparison between the energy optimization results through LOCC-VQE and unitary VQE with depth two circuits. (b) Comparison between the quantum mutual information between subsystems  $A$  and  $C$  as shown in Fig. 2 (a),  $I(A:C) = S(A) + S(C) - S(AC)$ , where  $S(\cdot)$  is the von Neumann entropy.

Our results suggest LOCC-VQE’s advantages over its unitary counterpart with the same depth in predicting ground state energy and quantum mutual information, as shown in Fig. 3. For ground state energy, LOCC-VQE can achieve a relative accuracy of  $10^{-3}$  in any perturbation direction over the entire range of perturbation intensity, while unitary VQE can only achieve a relative accuracy of  $10^{-1}$ , as shown in Fig. 3 (a). A precision gap of two orders of magnitude between LOCC-VQE and its unitary counterpart is demonstrated when the perturbation intensity  $\lambda$  in Eq. (5) is small, where long-range entanglement dominates the target ground state. To further demonstrate a provable advantage, we use quantum mutual information (QMI) between subsystems  $A$  and  $C$  to characterize long-range entanglement and thereby separate LOCC-VQE and its unitary counterpart. Theoretically, given a unitary circuit depth, the QMI vanishes outside of the light cones of information propagation. As shown in Fig. 3 (b), states prepared by LOCC-VQE have a non-zero QMI, the amount of which matches the ground state, while QMI is exactly zero for unitary VQE of the same circuit depth. This implies the advantage of LOCC-VQE originated from the ability to break the light cone of information propagation. The details of light-cone arguments



are available in Appendix D 2, and results of perturbation in other directions are demonstrated in Appendix F 1.

Strictly speaking, the  $n$ -qubit tensor product Pauli- $X$  term in Eq. (5) does not satisfy the local Hamiltonian condition in Theorem 1. Interestingly, our numerical results of LOCC-VQE can still prepare the ground state with high precision, as shown above. This implies LOCC-VQE's potential to work well even when conditions in Theorem 1 are relaxed. In a similar model without such a long-range term, the 1D transverse-field Ising model, we have also demonstrated the accurate results of the ground state preparation, whose Hamiltonian satisfies the local condition in Theorem 1, as shown in Appendix F 2,

### B. Perturbed rotated surface code

The ground states of the surface code Hamiltonian possess long-range entanglement, enabling the storage of logical information. In our numerical tests, we use the rotated surface code [38–42], which is a variant of Kiteav's toric code [3, 4] with open boundary condition. Consider the perturbation of a magnetic field in the  $Z$  direction, which results in the following Hamiltonian:

$$\hat{H}_{\text{sur}}(\lambda) = -(1-\lambda) \sum_v A_v - (1-\lambda) \sum_p B_p - \lambda \sum_{i=1}^{N_x N_y} Z_i. \quad (6)$$

In this model, the qubits are arranged in a regular lattice, as shown in Fig. 2 (b). Here,  $N_x$  and  $N_y$  represent the width and height of the regular lattice, respectively.  $A_v$  and  $B_p$  are stabilizers for the unperturbed rotated surface code, while  $\lambda$  represents the strength of the perturbation. The  $Z$ -type stabilizers  $A_v$  and the  $X$ -type stabilizers  $B_p$  are arranged in an alternating checkerboard pattern. The purpose of highlighting  $X$ -type and  $Z$ -type ancillary qubits in Fig. 2 (b) is to illustrate the model better, and we do not distinguish them in our numerical experiments, treating them equally when initializing parameters. The robustness and flexibility of LOCC-VQE make it possible to achieve high precision in ground-state preparation without requiring prior knowledge of the type of ancillary qubits.

The results of preparing ground states of perturbed rotated surface code using LOCC-VQE are shown in Fig. 4. LOCC-VQE can reach a relative error of  $10^{-2}$  in energy precision for all perturbation intensity. Even with a limited lattice size, where the effect of long-range entanglement on the estimated ground state energy is not as strong as in larger lattice sizes, a precision gap of three orders of magnitude between the ground states prepared by

LOCC-VQE and unitary VQE is demonstrated, as shown in Fig. 4, when the perturbation intensity  $\lambda$  in Eq. (6) is small, demonstrating the advantage of LOCC-VQE.

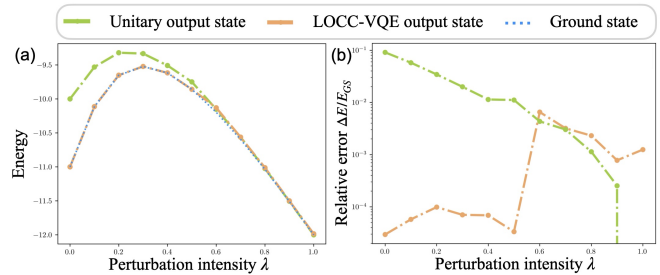


FIG. 4: Numerical simulation results of perturbed surface code. (a) Comparison between the energy optimization results through LOCC-VQE and unitary VQE with depth four circuits. (b) Comparison between the relative error of ground state energy optimization results,  $\frac{\Delta E}{E_{GS}} = \frac{E - E_{GS}}{E_{GS}}$ , through LOCC-VQE and unitary VQE with depth four circuits.

## V. DISCUSSION

In future work, various promising ways to enhance LOCC-VQE will be explored. For instance, one could employ architecture search [43] on circuits and LOCC protocols to discover better LOCC-assisted circuit ansatz. One could also further combine our approach with classical computations, such as tensor-network methods [44, 45]. From a theoretical perspective, the conditions in Theorem 1 could be relaxed to allow gradient decrease to some extent at the asymptotical limit while still preserving trainability. The trainability in finite size systems is also worth further exploration.

With recent advancements in quantum device capabilities, particularly in mid-circuit measurements, LOCC-assisted circuits have become experimentally feasible, as demonstrated on ion-trap platforms [46–48] and superconducting platforms [49, 50]. In our numerical simulations, the number of qubits used is within the capability of today's quantum computers, making experimental demonstrations already feasible. When running on a quantum computer, the computationally intensive part of LOCC-VQE will be greatly accelerated, enabling larger-scale experiments. We anticipate that such larger-scale experiments will unlock the full potential of LOCC-VQE in preparing long-range entangled states for quantum error correction, topological phases of matter and algorithms.

[1] X.-G. Wen, Topological Order: From Long-Range Entangled Quantum Matter to a Unified Origin of Light and Electrons, *International Scholarly Research Notices*

2013, e198710 (2013).

[2] X. Chen, Z.-C. Gu, and X.-G. Wen, Local unitary transformation, long-range quantum entanglement, wave func-

- tion renormalization, and topological order, *Physical Review B* **82**, 155138 (2010).
- [3] S. B. Bravyi and A. Y. Kitaev, *Quantum codes on a lattice with boundary* (1998), [arXiv:quant-ph/9811052](#).
- [4] A. Yu. Kitaev, Fault-tolerant quantum computation by anyons, *Annals of Physics* **303**, 2 (2003).
- [5] J. Yi, W. Ye, D. Gottesman, and Z.-W. Liu, Complexity and order in approximate quantum error-correcting codes (2023), [arXiv:2310.04710 \[cond-mat, physics:hep-th, physics:math-ph, physics:quant-ph\]](#).
- [6] D. Aharonov, M. Ben-Or, R. Impagliazzo, and N. Nisan, Limitations of Noisy Reversible Computation (1996), [arXiv:quant-ph/9611028](#).
- [7] A. Müller-Hermes, D. Stilck França, and M. M. Wolf, Relative entropy convergence for depolarizing channels, *Journal of Mathematical Physics* **57**, 022202 (2016).
- [8] Y. Yan, Z. Du, J. Chen, and X. Ma, *Limitations of Noisy Quantum Devices in Computational and Entangling Power* (2023), [arXiv:2306.02836 \[quant-ph\]](#).
- [9] A. J. Friedman, C. Yin, Y. Hong, and A. Lucas, *Locality and error correction in quantum dynamics with measurement* (2022), [arXiv:2206.09929 \[cond-mat, physics:math-ph, physics:quant-ph\]](#).
- [10] R. Raussendorf, S. Bravyi, and J. Harrington, Long-range quantum entanglement in noisy cluster states, *Physical Review A* **71**, 062313 (2005).
- [11] M. Aguado, G. K. Brennen, F. Verstraete, and J. I. Cirac, Creation, Manipulation, and Detection of Abelian and Non-Abelian Anyons in Optical Lattices, *Physical Review Letters* **101**, 260501 (2008).
- [12] L. Piroli, G. Styliaris, and J. I. Cirac, Quantum Circuits Assisted by Local Operations and Classical Communication: Transformations and Phases of Matter, *Physical Review Letters* **127**, 220503 (2021).
- [13] N. Tantivasadakarn, R. Thorngren, A. Vishwanath, and R. Verresen, Long-Range Entanglement from Measuring Symmetry-Protected Topological Phases, *Physical Review X* **14**, 021040 (2024).
- [14] S. Bravyi, I. Kim, A. Kliesch, and R. Koenig, *Adaptive constant-depth circuits for manipulating non-abelian anyons* (2022), [arXiv:2205.01933 \[quant-ph\]](#).
- [15] N. Tantivasadakarn, R. Verresen, and A. Vishwanath, Shortest Route to Non-Abelian Topological Order on a Quantum Processor, *Physical Review Letters* **131**, 060405 (2023).
- [16] N. Tantivasadakarn, A. Vishwanath, and R. Verresen, Hierarchy of Topological Order From Finite-Depth Unitaries, Measurement, and Feedforward, *PRX Quantum* **4**, 020339 (2023).
- [17] Y. Li, H. Suku, A. P. Mana, H. P. Nautrup, and T.-C. Wei, Symmetry-enriched topological order from partially gauging symmetry-protected topologically ordered states assisted by measurements, *Physical Review B* **108**, 115144 (2023).
- [18] G.-Y. Zhu, N. Tantivasadakarn, A. Vishwanath, S. Trebst, and R. Verresen, Nishimori's Cat: Stable Long-Range Entanglement from Finite-Depth Unitaries and Weak Measurements, *Physical Review Letters* **131**, 200201 (2023).
- [19] H. Buhrman, M. Folkertsma, B. Loff, and N. M. P. Neumann, State preparation by shallow circuits using feed forward (2023), [arXiv:2307.14840 \[quant-ph\]](#).
- [20] L. Piroli, G. Styliaris, and J. I. Cirac, *Approximating many-body quantum states with quantum circuits and measurements* (2024), [arXiv:2403.07604 \[cond-mat, physics:quant-ph\]](#).
- [21] T.-C. Lu, L. A. Lessa, I. H. Kim, and T. H. Hsieh, Measurement as a Shortcut to Long-Range Entangled Quantum Matter, *PRX Quantum* **3**, 040337 (2022).
- [22] K. C. Smith, E. Crane, N. Wiebe, and S. M. Girvin, Deterministic constant-depth preparation of the AKLT state on a quantum processor using fusion measurements (2022), [arXiv:2210.17548 \[cond-mat, physics:quant-ph\]](#).
- [23] D. Malz, G. Styliaris, Z.-Y. Wei, and J. I. Cirac, Preparation of Matrix Product States with Log-Depth Quantum Circuits, *Physical Review Letters* **132**, 040404 (2024).
- [24] K. C. Smith, A. Khan, B. K. Clark, S. M. Girvin, and T.-C. Wei, Constant-depth preparation of matrix product states with adaptive quantum circuits (2024), [arXiv:2404.16083 \[quant-ph\]](#).
- [25] D. Gunn, G. Styliaris, T. Kraft, and B. Kraus, *Phases of Matrix Product States with Symmetric Quantum Circuits and Symmetric Measurements with Feedforward* (2023), [arXiv:2312.13838 \[quant-ph\]](#).
- [26] A. Peruzzo, J. McClean, P. Shadbolt, M.-H. Yung, X.-Q. Zhou, P. J. Love, A. Aspuru-Guzik, and J. L. O'Brien, A variational eigenvalue solver on a photonic quantum processor, *Nature Communications* **5**, 4213 (2014).
- [27] P. J. J. O'Malley, R. Babbush, I. D. Kivlichan, J. Romero, J. R. McClean, R. Barends, J. Kelly, P. Roushan, A. Tranter, N. Ding, B. Campbell, Y. Chen, Z. Chen, B. Chiaro, A. Dunsworth, *et al.*, Scalable Quantum Simulation of Molecular Energies, *Physical Review X* **6**, 031007 (2016).
- [28] A. Kandala, A. Mezzacapo, K. Temme, M. Takita, M. Brink, J. M. Chow, and J. M. Gambetta, Hardware-efficient variational quantum eigensolver for small molecules and quantum magnets, *Nature* **549**, 242 (2017).
- [29] Google AI Quantum and Collaborators, F. Arute, K. Arya, R. Babbush, D. Bacon, J. C. Bardin, R. Barends, S. Boixo, M. Broughton, B. B. Buckley, D. A. Buell, B. Burkett, N. Bushnell, Y. Chen, Z. Chen, *et al.*, Hartree-Fock on a superconducting qubit quantum computer, *Science* **369**, 1084 (2020).
- [30] M. Cerezo, A. Arrasmith, R. Babbush, S. C. Benjamin, S. Endo, K. Fujii, J. R. McClean, K. Mitarai, X. Yuan, L. Cincio, and P. J. Coles, Variational quantum algorithms, *Nature Reviews Physics* **3**, 625 (2021).
- [31] R. R. Ferguson, L. Dellantonio, A. A. Balushi, K. Jansen, W. Dür, and C. A. Muschik, Measurement-Based Variational Quantum Eigensolver, *Physical Review Letters* **126**, 220501 (2021).
- [32] S. Guo, J. Sun, H. Qian, M. Gong, Y. Zhang, F. Chen, Y. Ye, Y. Wu, S. Cao, K. Liu, C. Zha, C. Ying, Q. Zhu, H.-L. Huang, Y. Zhao, *et al.*, Experimental quantum computational chemistry with optimized unitary coupled cluster ansatz, *Nature Physics* **10.1038/s41567-024-02530-z** (2024).
- [33] J. R. McClean, S. Boixo, V. N. Smelyanskiy, R. Babbush, and H. Neven, Barren plateaus in quantum neural network training landscapes, *Nature Communications* **9**, 4812 (2018).
- [34] H.-K. Zhang, S. Liu, and S.-X. Zhang, Absence of Barren Plateaus in Finite Local-Depth Circuits with Long-Range Entanglement, *Physical Review Letters* **132**, 150603 (2024).
- [35] S. Wang, E. Fontana, M. Cerezo, K. Sharma, A. Sone,

- L. Cincio, and P. J. Coles, Noise-induced barren plateaus in variational quantum algorithms, *Nature Communications* **12**, 6961 (2021).
- [36] S.-X. Zhang, J. Allcock, Z.-Q. Wan, S. Liu, J. Sun, H. Yu, X.-H. Yang, J. Qiu, Z. Ye, Y.-Q. Chen, C.-K. Lee, Y.-C. Zheng, S.-K. Jian, H. Yao, C.-Y. Hsieh, *et al.*, Tensor-Circuit: A Quantum Software Framework for the NISQ Era, *Quantum* **7**, 912 (2023).
- [37] <https://github.com/Marsmmz/LOCC-VQE.git>.
- [38] H. Bombin and M. A. Martin-Delgado, Optimal resources for topological two-dimensional stabilizer codes: Comparative study, *Physical Review A* **76**, 012305 (2007).
- [39] A. A. Kovalev and L. P. Pryadko, Improved quantum hypergraph-product LDPC codes, in *2012 IEEE International Symposium on Information Theory Proceedings* (2012) pp. 348–352.
- [40] A. G. Fowler, M. Mariantoni, J. M. Martinis, and A. N. Cleland, Surface codes: Towards practical large-scale quantum computation, *Physical Review A* **86**, 032324 (2012).
- [41] J. T. Anderson, Homological stabilizer codes, *Annals of Physics* **330**, 1 (2013).
- [42] Y. Tomita and K. M. Svore, Low-distance surface codes under realistic quantum noise, *Physical Review A* **90**, 062320 (2014).
- [43] S.-X. Zhang, C.-Y. Hsieh, S. Zhang, and H. Yao, Differentiable Quantum Architecture Search (2021), [arXiv:2010.08561](https://arxiv.org/abs/2010.08561) [quant-ph].
- [44] X. Yuan, J. Sun, J. Liu, Q. Zhao, and Y. Zhou, Quantum Simulation with Hybrid Tensor Networks, *Physical Review Letters* **127**, 040501 (2021).
- [45] J. Huang, W. He, Y. Zhang, Y. Wu, B. Wu, and X. Yuan, Tensor-network-assisted variational quantum algorithm, *Physical Review A* **108**, 052407 (2023).
- [46] M. Foss-Feig, A. Tikku, T.-C. Lu, K. Mayer, M. Iqbal, T. M. Gatterman, J. A. Gerber, K. Gilmore, D. Gresh, A. Hankin, N. Hewitt, C. V. Horst, M. Matheny, T. Mengle, B. Neyenhuis, *et al.*, Experimental demonstration of the advantage of adaptive quantum circuits (2023), [arXiv:2302.03029](https://arxiv.org/abs/2302.03029) [cond-mat, physics:quant-ph].
- [47] M. Iqbal, N. Tantivasadakarn, T. M. Gatterman, J. A. Gerber, K. Gilmore, D. Gresh, A. Hankin, N. Hewitt, C. V. Horst, M. Matheny, T. Mengle, B. Neyenhuis, A. Vishwanath, M. Foss-Feig, R. Verresen, *et al.*, Topological order from measurements and feed-forward on a trapped ion quantum computer, *Communications Physics* **7**, 205 (2024).
- [48] S. A. Moses, C. H. Baldwin, M. S. Allman, R. Ancona, L. Ascarrunz, C. Barnes, J. Bartolotta, B. Bjork, P. Blanchard, M. Bohn, J. G. Bohnet, N. C. Brown, N. Q. Burdick, W. C. Burton, S. L. Campbell, *et al.*, A Race-Track Trapped-Ion Quantum Processor, *Physical Review X* **13**, 041052 (2023).
- [49] E. Bäumer, V. Tripathi, D. S. Wang, P. Rall, E. H. Chen, S. Majumder, A. Seif, and Z. K. Mineev, Efficient Long-Range Entanglement using Dynamic Circuits (2023), [arXiv:2308.13065](https://arxiv.org/abs/2308.13065) [quant-ph].
- [50] A. D. Córcoles, M. Takita, K. Inoue, S. Lekuch, Z. K. Mineev, J. M. Chow, and J. M. Gambetta, Exploiting Dynamic Quantum Circuits in a Quantum Algorithm with Superconducting Qubits, *Physical Review Letters* **127**, 100501 (2021).

## Appendix A: Formal definitions

Here, we revisit the definition of LOCC-assisted circuits [12] and formalize it in the following way.

**Definition 1** (LOCC-assisted circuits). *Starting from the initial state  $|\Psi_0\rangle$ , we alternatively apply unitaries or measurements. Assumed that the outcomes are  $\mathbf{v} = \{v_j\}$ , the unnormalized outcome state with respect to the outcome  $\mathbf{v} = \{v_j\}$  will be*

$$|\tilde{\Phi}_{\mathbf{v}}\rangle = U_{\mathbf{v}}^{(d)} \Pi_{\mathbf{v}}^{(d-1)} \dots \Pi_{\mathbf{v}}^{(1)} U^{(1)} |\Psi_0\rangle. \quad (\text{A1})$$

Here,  $U_{\mathbf{v}}^{(i)}$  denotes unitaries, and  $\Pi_{\mathbf{v}}^{(i)}$  denotes measurement projectors. Unitaries  $U_{\mathbf{v}}^{(i)}$  may depend on earlier measurement outcomes corresponding to projectors  $\Pi_j$  for  $j < i$ . The LOCC-assisted circuits, on average, will generate the following state:

$$\Psi = \sum_{\mathbf{v}} |\tilde{\Phi}_{\mathbf{v}}\rangle \langle \tilde{\Phi}_{\mathbf{v}}|. \quad (\text{A2})$$

The depth of LOCC-assisted circuits is the sum of all unitary layers, as defined below.

**Definition 2** (Depth of a LOCC-assisted circuit). *The depth of a LOCC-assisted circuit is the sum of the depths of  $U_{\mathbf{v}}^{(i)}$  in Eq. (A1). The depth of each  $U_{\mathbf{v}}^{(i)}$ , denoted by  $d_i$ , is defined as the following: Decompose the unitary by  $d_i$  layers of gates  $\prod_{j=1}^{d_i} \otimes_k U_{j,k}^{(i)}$ , where within a same layer, labelled by  $j$ ,  $U_{j,k}^{(i)}$  are two-qubit unitaries that do not overlap with each other.*

## Appendix B: Proofs and details of gradient estimation protocol

Our gradient estimation protocol is built on Proposition 1, for which we give proof below.

*Proof of Proposition 1.*

$$\begin{aligned} \frac{\partial \text{Tr} [\hat{H} \Psi_{\gamma}]}{\partial \gamma_j} &= \sum_{\mathbf{v}} \frac{\partial}{\partial \gamma_j} \text{Tr} [\hat{H} \tilde{\Phi}_{\theta, \mathbf{v}}] \\ &= \sum_{i, \mathbf{v}} \frac{\partial g_i(\gamma, \mathbf{v})}{\partial \gamma_j} \frac{\partial \text{Tr} [\hat{H} \tilde{\Phi}_{\theta, \mathbf{v}}]}{\partial \theta_i} \Big|_{\theta=g(\gamma, \mathbf{v})} \\ &= \sum_{i, \mathbf{v}} \frac{1}{2} \frac{\partial g_i(\gamma, \mathbf{v})}{\partial \gamma_j} \left( \text{Tr} [\hat{H} \tilde{\Phi}_{\theta, \mathbf{v}}] \Big|_{\theta=g_{i+}(\gamma, \mathbf{v})} - \text{Tr} [\hat{H} \tilde{\Phi}_{\theta, \mathbf{v}}] \Big|_{\theta=g_{i-}(\gamma, \mathbf{v})} \right) \\ &= \sum_{i, \mathbf{v}} \frac{1}{2} \frac{\partial g_i(\gamma, \mathbf{v})}{\partial \gamma_j} \left( P_{\theta=g_{i+}(\gamma, \mathbf{v})}(\mathbf{v}) \text{Tr} [\hat{H} \Phi_{\theta, \mathbf{v}}] \Big|_{\theta=g_{i+}(\gamma, \mathbf{v})} - P_{\theta=g_{i-}(\gamma, \mathbf{v})}(\mathbf{v}) \text{Tr} [\hat{H} \Phi_{\theta, \mathbf{v}}] \Big|_{\theta=g_{i-}(\gamma, \mathbf{v})} \right). \end{aligned} \quad (\text{B1})$$

The third equality uses parameter shifts for quantum gradients. Unlike unitary variational circuits, we adapt parameter shifts to circuits with projectors as detailed in Lemma 1.  $\square$

**Lemma 1** (Parameter shifts with mid-circuit measurements).

$$\frac{\partial \text{Tr} [\hat{H} \tilde{\Phi}_{\theta, \mathbf{v}}]}{\partial \theta_i} = \frac{1}{2} \left( \text{Tr} [\hat{H} \tilde{\Phi}_{\theta + \frac{\pi}{2} \mathbf{e}_i, \mathbf{v}}] - \text{Tr} [\hat{H} \tilde{\Phi}_{\theta - \frac{\pi}{2} \mathbf{e}_i, \mathbf{v}}] \right). \quad (\text{B2})$$

*Proof.* By Eq. (A1),

$$\tilde{\Phi}_{\theta, \mathbf{v}} = U^{(d)} \Pi^{(d-1)} \dots \Pi^{(1)} U^{(1)} |\Psi_0\rangle \langle \Psi_0| (U^{(1)})^\dagger \Pi^{(1)} \dots \Pi^{(d-1)} (U^{(d)})^\dagger, \quad (\text{B3})$$

where we omit the subscript  $\mathbf{v}$  for simplicity.



Express  $U^{(k)}$  as  $U^{(k)} = VW(\theta_i)V'$ , where  $W(\theta_i) = e^{-i\frac{\theta_i}{2}\Sigma_i}$ ,  $\Sigma_i$  is a Pauli operator and  $\theta_i$  is assumed to act non-trivially on  $U^{(k)}$ . Note that

$$\begin{aligned}\frac{\partial U^{(k)}}{\partial \theta_i} &= -\frac{i}{2}V\Sigma_iW(\theta_i)V', \\ \frac{\partial (U^{(k)})^\dagger}{\partial \theta_i} &= \frac{i}{2}(V')^\dagger\Sigma_iW(-\theta_i)V^\dagger.\end{aligned}\tag{B4}$$

Then, we calculate the gradient,

$$\begin{aligned}\frac{\partial \text{Tr} [\hat{H}\tilde{\Phi}_{\theta,\mathbf{v}}]}{\partial \theta_i} &= \text{Tr} \left[ \hat{H}U^{(d)}\Pi^{(d-1)} \dots \frac{\partial U^{(k)}}{\partial \theta_i} \dots \Pi^{(1)}U^{(1)}|\Psi_0\rangle\langle\Psi_0|(U^{(1)})^\dagger\Pi^{(1)} \dots \Pi^{(d-1)}(U^{(d)})^\dagger + h.c. \right] \\ &= -\frac{i}{2}\text{Tr} \left[ \hat{H}U^{(d)}\Pi^{(d-1)} \dots VW(\theta_i)[\Sigma_i, \rho]W(-\theta_i)V^\dagger \dots \Pi^{(d-1)}(U^{(d)})^\dagger \right].\end{aligned}\tag{B5}$$

where  $\rho = V'U^{(i-1)}\Pi^{(i-2)} \dots \Pi^{(1)}U^{(1)}|\Psi_0\rangle\langle\Psi_0|(U^{(1)})^\dagger\Pi^{(1)} \dots \Pi^{(i-2)}(U^{(i-1)})^\dagger(V')^\dagger$ .

Further, using the fact that  $[\Sigma_j, \rho] = i[W(\frac{\pi}{2})\rho W(\frac{\pi}{2})^\dagger - W(-\frac{\pi}{2})\rho W(-\frac{\pi}{2})^\dagger]$ , we have

$$\begin{aligned}\frac{\partial \text{Tr} [\hat{H}\tilde{\Phi}_{\theta,\mathbf{v}}]}{\partial \theta_i} &= -\frac{i}{2}\text{Tr} \left[ \hat{H}U^{(d)}\Pi^{(d-1)} \dots VW(\theta_i) \left[ W(\frac{\pi}{2})\rho W(\frac{\pi}{2})^\dagger - W(-\frac{\pi}{2})\rho W(-\frac{\pi}{2})^\dagger \right] W(-\theta_i)V^\dagger \dots \Pi^{(d-1)}(U^{(d)})^\dagger \right] \\ &= U^{(d)}\Pi^{(d-1)} \dots \Pi^{(1)}U^{(1)}|\Psi_0\rangle\langle\Psi_0|(U^{(1)})^\dagger\Pi^{(1)} \dots \Pi^{(d-1)}(U^{(d)})^\dagger.\end{aligned}\tag{B6}$$

Compared with the usual quantum gradient, the lemma considers circuits with projectors as the consequence of measurements. The proof above shows that projectors do not affect the quantum gradients for unitary circuits.  $\square$

As explained in the main text, Proposition 1 implies the gradient can be obtained as a combination of quantum and classical parts. The detailed algorithm is given below.

---

**Algorithm 1:** Gradient estimation protocol for LOCC-VQE

---

**Data:** Observable  $\hat{H}$ ; ansatz  $\Psi_\gamma$  defined by  $g(\gamma, \mathbf{v})$ ; estimation sample rounds  $M$ .

**Result:** Estimated gradient  $\{G_j\}_{j=1, \dots, |\gamma|}$ .

**for**  $i \leftarrow 1$  **to**  $|\theta|$  **do**

$g_{i\pm}(\gamma, \mathbf{v}) \leftarrow g(\gamma, \mathbf{v}) \pm \frac{\pi}{2}\mathbf{e}_i$ ;

$\mathcal{C}_{i+} \leftarrow \emptyset$ ;

**for**  $k \leftarrow 1$  **to**  $M$  ;

**do**

Run the LOCC-assisted circuit using  $g_+$ ;

$\mathbf{v} \leftarrow$  mid-circuit measurement results;

$c \leftarrow$  one-shot estimation of  $\hat{H}$  using  $g_+$ ;

Add the pair,  $(\mathbf{v}, c)$ , to  $\mathcal{C}_{i+}$ ;

Do the same procedure to get  $\mathcal{C}_{i-}$  from  $g_-$ ;

**for**  $j \leftarrow 1$  **to**  $|\gamma|$  **do**

$G_+ \leftarrow 0$ ;

$G_- \leftarrow 0$ ;

**for**  $i \leftarrow 1$  **to**  $|\theta|$  **do**

**for**  $(\mathbf{v}, c) \in \mathcal{C}_{i+}$  **do**

$G_+ \leftarrow G_+ + \frac{1}{2} \frac{\partial g_i(\gamma, \mathbf{v})}{\partial \gamma_j} c$ ;

**for**  $(\mathbf{v}, c) \in \mathcal{C}_{i-}$  **do**

$G_- \leftarrow G_- + \frac{1}{2} \frac{\partial g_i(\gamma, \mathbf{v})}{\partial \gamma_j} c$ ;

$G_j \leftarrow \frac{1}{M|\theta|}(G_+ - G_-)$ ;

/\*  $|\cdot|$  denotes the parameter vector length \*/

/\* quantum computer \*/

---

## Appendix C: Proof of the absence of barren plateaus

### 1. Quantum gradients for variational LOCC-assisted circuits

As we have shown in Proposition 1, the quantum gradients for variational LOCC-assisted circuits can be expressed as:

$$\begin{aligned} \frac{\partial \text{Tr} [\hat{H} \Psi_\gamma]}{\partial \gamma_k} &= \sum_{\mathbf{v}} \frac{\partial}{\partial \gamma_k} \text{Tr} [\hat{H} \tilde{\Phi}_{\theta, \mathbf{v}}] \\ &= \sum_{i, \mathbf{v}} \frac{\partial g_i(\gamma, \mathbf{v})}{\partial \gamma_k} \frac{\partial \text{Tr} [\hat{H} \tilde{\Phi}_{\theta, \mathbf{v}}]}{\partial \theta_i} \Bigg|_{\theta=g(\gamma, \mathbf{v})} \end{aligned} \quad (\text{C1})$$

Denote the length of  $\theta$  as  $l$ , the length of  $\mathbf{v}$  as  $m$ . Let the matrix representing the quantum gradients be  $\mathbf{G}^{Q_k} \in \mathbb{R}^{l \times 2^m}$ , calculated by parameter-shift, and the matrix representing the classical gradients be  $\mathbf{G}^{C_k} \in \mathbb{R}^{l \times 2^m}$ :

$$\begin{aligned} \mathbf{G}^{Q_k} &= \{g_{i,j}^{Q_k}\} = \left\{ \frac{\partial \text{Tr} [\hat{H} \tilde{\Phi}_{\theta, \mathbf{v}_i}]}{\partial \theta_j} \Bigg|_{\theta_j=g_j(\gamma, \mathbf{v}_i)} \right\} \\ \mathbf{G}^{C_k} &= \{g_{i,j}^{C_k}\} = \left\{ \frac{\partial g_j(\gamma, \mathbf{v}_i)}{\partial \gamma_k} \right\} \end{aligned} \quad (\text{C2})$$

where  $\mathbf{v}_i$  is a bit string of length  $m$  representing the  $i^{\text{th}}$  possible way of projectors.

We can rewrite the quantum gradient for variational LOCC-assisted circuits as:

$$\frac{\partial \text{Tr} [\hat{H} \Psi_\gamma]}{\partial \gamma_k} = \langle \mathbf{G}^{C_k}, \mathbf{G}^{Q_k} \rangle_F = \text{Tr} [(\mathbf{G}^{C_k})^T \mathbf{G}^{Q_k}] \quad (\text{C3})$$

where  $\langle \cdot, \cdot \rangle_F$  is the Frobenius inner product, which can be seen as the inner product of the vectorized representation of  $(\mathbf{G}^{C_k})^T$  and  $(\mathbf{G}^{Q_k})^T$ .

### 2. Notations and interpretations of Theorem 1

The first condition **A1** in Theorem 1 set each term in  $\hat{H}$  only affect at most  $\kappa = \mathcal{O}(1)$  local qubits. If  $\hat{H} = \hat{H}_1 + \hat{H}_2 + \dots + \hat{H}_M$ ,  $\kappa := \max(|\text{supp}(\hat{H}_i)|) = \mathcal{O}(1)$ .

The second condition **A2** in Theorem 1 states that the LOCC circuit has constant depth  $d = \mathcal{O}(1)$ . Here, the depth of the circuit follows Definition 2. The third condition **A3** in Theorem 1 ensures the classical gradients do not vanish. The last two conditions **A4** and **A5** in Theorem 1 are less intuitive at first encounter. It means that for all  $l$  outputs of the classical function  $g$ , each parameter  $\gamma$  at most affects  $\iota = \mathcal{O}(1)$  of them. Meanwhile, each of the  $l$  outputs is only controlled by  $\nu = \mathcal{O}(1)$  input measurement results.

Due to the inner product structure as shown in Proposition 1, we consider the worst case where the vectorized representation of  $(\mathbf{G}^{C_k})^T$  and  $(\mathbf{G}^{Q_k})^T$  are uniformly distributed on the unit sphere in  $\mathbb{R}^{\mathcal{D}}$  where  $\mathcal{D}$  can be seen as the degree of freedom of the result with inner product structure.

### 3. Backward light cone

We first introduce the light cone perspective of how information propagates through quantum circuits [9], which is illustrated in Fig. 5. From the Heisenberg picture, the evolution of a quantum state can be seen as a reversed transform of the observable. Suppose the initial state is  $|\psi_i\rangle$ , the unitary circuit is  $U$ , and the observable is  $O$ . Then the output state  $|\psi_o\rangle$  is:

$$|\psi_o\rangle = U |\psi_i\rangle. \quad (\text{C4})$$

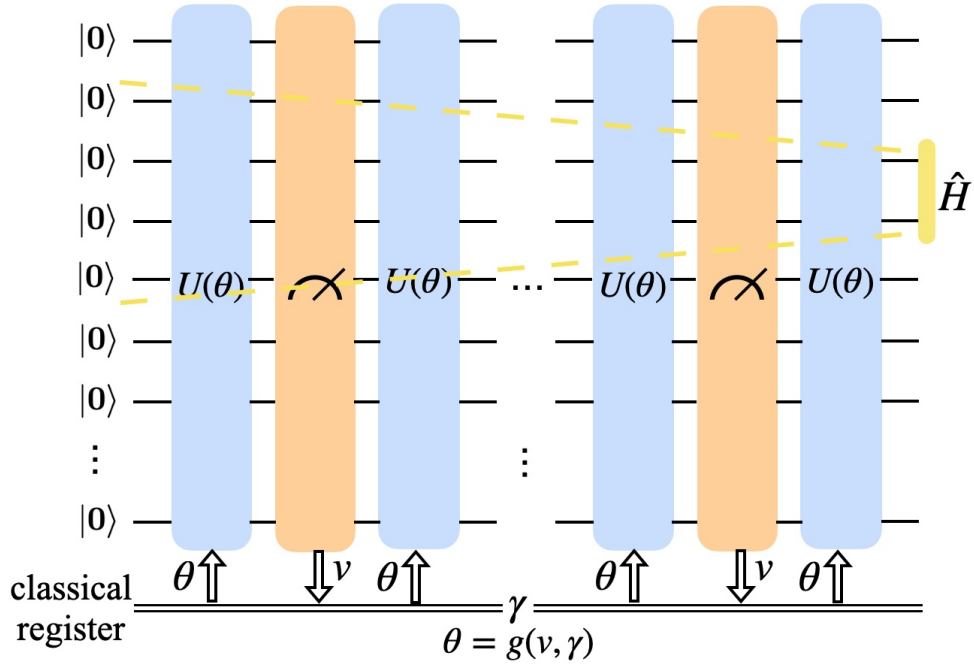


FIG. 5: Backward light cone of a local Hamiltonian. The dashed yellow line represents the backward light cone of a local Hamiltonian  $\hat{H}$ , with the support of  $\hat{H}$  represented by the vertical yellow bar, containing a constant number of qubits.

The expectation value of the observable on the output state is:

$$\langle O \rangle = \langle \psi_o | O | \psi_o \rangle = \langle \psi_i | U^\dagger O U | \psi_i \rangle, \quad (\text{C5})$$

which can also be viewed as taking the expectation value of the observable  $\tilde{O} = U^\dagger O U | \psi_i \rangle$  on the input state  $|\psi_i\rangle$ . From a quantum circuit perspective, if  $U$  consists of local two-qubit unitary gates, then the size of the set of qubits affected by the observable will increase linearly with the depth of the circuit. Therefore, the information of a local observable will be affected by  $\mathcal{O}(d)$  qubits, where  $d$  is the depth of the local two-qubit gates in the unitary circuit. With the conditions in Theorem 1, we are able to prove sparse structures of quantum and classical gradient matrices. With the inner product structures, the sparsity will lead to proving that the degree of freedom  $\mathcal{D} = \mathcal{O}(1)$  and eventually lower bound the gradient of LOCC-VQE by a constant independent of  $n$ .

#### 4. Proof of Theorem 1

For simplicity, in the following proof, we focus on the case that  $\hat{H}$  has only one term. We can add them if multiple terms are in  $\hat{H}$ .

##### a. Proof outline

The conditions in the previous section can guarantee that both  $\mathbf{G}^{Q_k}$  and  $\mathbf{G}^{C_k}$  are sparse, and the entries in these two matrices are not exponentially small.

For  $\mathbf{G}^{Q_k}$ , condition  $\mathcal{A1}$  and  $\mathcal{A2}$  can prevent the entries of  $\mathbf{G}^{Q_k}$  to be exponentially small, which avoid the barren plateaus phenomenon in the unitary VQE. At the same time, these two conditions can also guarantee that the number of different values in each row of  $\mathbf{G}^{Q_k}$  is a constant from a light cone perspective.

On the other hand, for  $\mathbf{G}^{C_k}$ , Condition  $\mathcal{A3}$  prevent the entries in  $\mathbf{G}^{C_k}$  to be exponentially small. Condition  $\mathcal{A4}$  guarantees that the number of non-zero rows of  $\mathbf{G}^{C_k}$  is a constant. Meanwhile, Condition  $\mathcal{A5}$  indicates that the number of different values in each row of  $\mathbf{G}^{C_k}$  is a constant.

With the inner product structure of the gradient of LOCC-VQE, the effective entries of  $\mathbf{G}^{Q_k}$  and  $\mathbf{G}^{C_k}$  that contribute to the result have only a constant degree of freedom, which eventually ensures LOCC-VQE is free of barren plateaus.

For  $\mathbf{G}^{C_k}$ , condition  $\mathcal{A4}$  will guarantee that only constant number of rows of  $\mathbf{G}^{C_k}$  are non-zero. For  $\mathbf{G}^{Q_k}$ , condition  $\mathcal{A1}$  and  $\mathcal{A2}$  will lead to a light cone argument, as illustrated in Fig. 5, upper bounding the number of different values in each row of  $\mathbf{G}^{Q_k}$  to be constant. This means that the degree of freedom of  $\mathbf{G}^{Q_k}$  is restricted, which is another form of sparsity. Along with condition  $\mathcal{A3}$ , the sparse structures of both  $\mathbf{G}^{C_k}$  and  $\mathbf{G}^{Q_k}$  can guarantee that, with high probability, the gradient  $\frac{\partial \text{Tr}[\hat{H}\Psi_\gamma]}{\partial \gamma_k}$  scales independently of  $n$ .

b. Proof details

**Lemma 2.** *The entries of  $\mathbf{G}^{Q_k}$  do not decay with  $n$  in the asymptotic limit.*

*Proof.* In Lemma 1, it has been proved that the quantum gradient can still be calculated with parameter shifts. With condition  $\mathcal{A1}$  and  $\mathcal{A2}$ , the circuit depth is constant, and the observable is local. From an information propagation light cone perspective, only a constant number of qubits view affects the gradient information with respect to each term in the Hamiltonian. This proved that each entry of  $\mathbf{G}^{Q_k}$  will only be affected by a constant number of qubits, which will not decay in the asymptotic limit.  $\square$

**Lemma 3.** *The number of projectors in the backward light cone of  $\hat{H}$  is constant.*

*Proof.* The proof is based on condition  $\mathcal{A1}$  and  $\mathcal{A2}$  with the light cone argument as illustrated in Fig. 5. Denote the support of the observable  $\hat{H}$  as  $S := \text{supp}(\hat{H})$ . Condition  $\mathcal{A1}$  states that  $\kappa = |S| = \mathcal{O}(1)$  and  $S$  follows the locality constraint. Denote the backward light cone of  $S$  as  $\mathcal{L}_S$ . In the following proof, we will focus on the special case where  $S$  is geometrically local to simplify notations. It immediately implies the original statement since  $S$  has a constant size. We will prove that the number of projectors in the light cone  $\mathcal{L}_S$  is constant.

We explicitly write  $S$  as:

$$S = \mathbf{q}[i, i + \kappa - 1] \quad (\text{C6})$$

due to the locality of  $\hat{H}$ , where  $\mathbf{q}[a, b]$  represent the set of qubits from the  $a^{\text{th}}$  qubit to the  $b^{\text{th}}$  qubit. Consider the  $j^{\text{th}}$  layer of 2-qubit gates, denote the set of qubits in the overlap between the  $j^{\text{th}}$  layer of 2-qubit gates of the circuit and light cone  $\mathcal{L}_S$  as  $\mathcal{Q}_{\mathcal{L}_S}^j$ . We have:

$$\mathcal{Q}_{\mathcal{L}_S}^j \subseteq \mathbf{q}[\max(0, i - (d - j)), \min(n, i + \kappa - 1 + (d - j))] \quad (\text{C7})$$

where  $d$  is the depth of the circuit. This is the direct result of the light cone propagation through the circuit. Consequently, there are at most  $|\mathcal{Q}_{\mathcal{L}_S}^j| \leq \kappa + 2(d - j)$  projectors in the  $j^{\text{th}}$  layer. Now we sum the number of projectors in all  $d$  layers up, and we can upper bound the number of projectors that will affect the expectation value of the observable  $\hat{H}$  by:

$$\sum_{j=1}^d |\mathcal{Q}_{\mathcal{L}_S}^j| \leq \sum_{j=1}^d (\kappa + 2(d - j)) = \kappa d + d(d + 1) = \mathcal{O}(1), \quad (\text{C8})$$

which completed the proof.  $\square$

**Lemma 4.** *The number of different values in each row of  $\mathbf{G}^{Q_k}$  is constant.*

*Proof.* For each quantum parameter  $\theta_i$ , corresponding to the  $i^{\text{th}}$  row  $\mathbf{G}^{Q_k}$ , we are doing partial derivative of  $\partial \text{Tr}[\hat{H}\Psi_\gamma]$  over  $\theta_i$ . This means that we need to fix all other quantum parameters during the calculation. Consider the entries in the  $i^{\text{th}}$  row of  $\mathbf{G}^{Q_k}$ , each entry corresponds to the gradient value when obtaining a possible measurement result. However, with all other parameters fixed, only the measurement outcomes in the backward light cone can affect the expectation value of  $\hat{H}$ . In other words, only the different measurement outcomes within the backward light cone of  $\hat{H}$  can contribute to having different values in the  $i^{\text{th}}$  row of  $\mathbf{G}^{Q_k}$ .

Denote the  $i^{\text{th}}$  row of  $\mathbf{G}^{Q_k}$  as  $\mathbf{g}_i^{Q_k}$ , and let  $\tilde{g}_i^{Q_k}$  be the set of all different values in  $\mathbf{g}_i^{Q_k}$ . Denote the size of  $\tilde{g}_i^{Q_k}$  as  $\zeta_i := |\tilde{g}_i^{Q_k}|$ .

With lemma 3, only a constant number of projectors affect the expectation value of the observable  $\hat{H}$ . Denote the number of projectors that affect the expectation value of the observable  $\hat{H}$  as  $\chi = \mathcal{O}(1)$ . Then, for any row  $i$  of  $\mathbf{G}^{Q_k}$ ,  $\zeta_i$  is upper bounded by  $2^\chi$ . Thus, we have

$$\zeta_i \leq 2^\chi = \mathcal{O}(1), \forall i \in [l], \quad (\text{C9})$$

which completed the proof.  $\square$

**Lemma 5.** *The number of non-zero rows of  $\mathbf{G}^{C_k}$ .*

*Proof.* Denote the support of the parameter  $\gamma_k$  as  $\text{supp}(\gamma_k)$ :

$$\text{supp}(\gamma_k) = \{\theta_{\gamma_k}^1, \{\theta_{\gamma_k}^2, \dots, \theta_{\gamma_k}^{\iota_k}\}\} \quad (\text{C10})$$

which is a subset of the outputs  $\theta$  of the classical function  $g$ . The size of  $\text{supp}(\gamma_k)$  is  $\iota_k = |\text{supp}(\gamma_k)| = \mathcal{O}(1)$ . For each output  $\theta_j = g_j(\gamma, \mathbf{v}_i)$ , if  $\theta_j \notin \text{supp}(\gamma_k)$ , we have:

$$g_{i,j}^{C_k} = \frac{\partial \theta_j}{\partial \gamma_k} = \frac{\partial g_j(\gamma, \mathbf{v}_i)}{\partial \gamma_k} = 0, \forall i \in [2^m].$$

Thus, all rows of  $\mathbf{G}^{C_k}$  that do not correspond to the support of  $\gamma_k$  are zero, resulting in only  $\iota_k = |\text{supp}(\gamma_k)| = \mathcal{O}(1)$  rows of  $\mathbf{G}^{C_k}$  are non-zero.  $\square$

**Lemma 6.** *The number of different values in each row of  $\mathbf{G}^{C_k}$  is constant*

*Proof.* With condition **A5**, the value of  $g_j$  is only relevant to  $\nu_j = \mathcal{O}(1)$  measurement results. So, the number of different values among the entries in the  $j$ th row of  $\mathbf{G}^{C_k}$  is at most  $2^{\nu_j} = \mathcal{O}(1)$  for all  $j$ .  $\square$

**Lemma 7.** *For two vectors  $\mathbf{a}, \mathbf{b} \in \mathbb{R}^D$ , such that  $\|\mathbf{a}\| = \|\mathbf{b}\| = 1$  uniformly sampled at random, and for any  $\eta \leq 0.1$ , the probability that the inner product of these two vector larger than  $\eta$  is lower bounded, i.e.  $\mathbb{P}(\langle \mathbf{a}, \mathbf{b} \rangle \geq \eta) \geq \Omega(e^{-(D-1)\eta} - 0.2^{\frac{D-1}{2}})$ .*

*Proof.* Consider a  $D$ -dimensional unit sphere  $\mathcal{B}^D \in \mathbb{R}^D$  with its center at the origin. We can restate this lemma as sampling two vectors  $\mathbf{a}$  and  $\mathbf{b}$  on  $\mathcal{B}^D$  uniformly at random, and the probability that their inner product is larger than  $\eta$  is lower bounded by  $\Omega(e^{-(D-1)\eta} - 0.2^{\frac{D-1}{2}})$ . Without loss of generality, we can set  $\mathbf{a} = \mathbf{e}_1$  which is a unit vector with only the first dimension non-zero, and we call its endpoint the north pole of  $\mathcal{B}^D$ .

Since the volume of a  $D$  dimensional sphere with radius  $R$  is:

$$V_D(R) = \frac{\pi^{D/2} R^D}{\Gamma(1 + D/2)}, \quad (\text{C11})$$

the volume of  $\mathcal{B}^D$  is

$$V(\mathcal{B}^D) = \frac{\pi^{D/2}}{\Gamma(1 + D/2)}. \quad (\text{C12})$$

Let the  $D - 1$  dimensional sphere  $\mathcal{E}_{\mathcal{B}^D} \subseteq \mathbb{R}^D$  with  $x_1 = 0$  be the equator of  $\mathcal{B}^D$ , and let  $\mathcal{B}_\eta^D$  be the area such that:

$$\begin{aligned} \mathcal{B}_\eta^D &\subseteq \mathcal{B}^D, \\ \forall p \in \mathcal{B}_\eta^D, q \in \mathcal{E}_{\mathcal{B}^D}, \min \mathfrak{d}(p, q) &\geq \eta \end{aligned} \quad (\text{C13})$$

where  $\mathfrak{d}(p, q)$  is the Euclidean distance between two points in  $\mathbb{R}^D$ , and  $\eta \leq 0.1$ . Note that this guarantees that  $\forall p \in \mathcal{B}_\eta^D$ , the coefficient corresponding to the first dimension is at least  $\eta$ . Therefore, the probability of the inner product of  $\mathbf{a}$  and  $\mathbf{b}$  larger than  $\eta$  is the ratio of the volume of  $\mathcal{B}_\eta^D$  and  $\mathcal{B}^D$ .

More explicitly, the volume of  $\mathcal{B}_\eta^D$  is:

$$\begin{aligned} V(\mathcal{B}_\eta^D) &= 2 \int_\eta^1 V_{D-1}(\sqrt{1-h^2}) dh \\ &= \frac{2\pi^{\frac{D-1}{2}}}{\Gamma(1 + \frac{D-1}{2})} \int_\eta^1 (1-h^2)^{\frac{D-1}{2}} dh \end{aligned} \quad (\text{C14})$$

To lower bound  $V(\mathcal{B}_\eta^D)$ , we introduce  $h^* \in (0.9, 1)$  such that  $1 - (h^*)^2 = e^{-2h^*}$ . This guarantees that:

$$1 - h^2 \geq e^{-2h}, \forall h \in (0, h^*). \quad (\text{C15})$$



So:

$$\begin{aligned}
V(\mathcal{B}_\eta^D) &= \frac{2\pi^{\frac{D-1}{2}}}{\Gamma(1 + \frac{D-1}{2})} \int_\eta^1 (1-h^2)^{\frac{D-1}{2}} dh \\
&\geq \frac{2\pi^{\frac{D-1}{2}}}{\Gamma(1 + \frac{D-1}{2})} \int_\eta^{h^*} (1-h^2)^{\frac{D-1}{2}} dh \\
&\geq \frac{2\pi^{\frac{D-1}{2}}}{\Gamma(1 + \frac{D-1}{2})} \int_\eta^{h^*} e^{-2h \cdot \frac{D-1}{2}} dh \\
&= \frac{2\pi^{\frac{D-1}{2}}}{\Gamma(1 + \frac{D-1}{2})} \int_\eta^{h^*} e^{-(D-1)h} dh \\
&= \frac{2\pi^{\frac{D-1}{2}}}{\Gamma(1 + \frac{D-1}{2})} \cdot \frac{1}{D-1} \cdot (e^{-(D-1)\eta} - e^{-(D-1)h^*}) \\
&= \frac{\pi^{\frac{D}{2}}}{\Gamma(1 + \frac{D-1}{2}) \cdot \frac{D-1}{2}} \cdot \frac{1}{\sqrt{\pi}} \cdot (e^{-(D-1)\eta} - (1 - (h^*)^2)^{\frac{D-1}{2}}) \\
&\geq \frac{\pi^{\frac{D}{2}}}{\Gamma(1 + \frac{D-1}{2}) \cdot \frac{D+1}{2}} \cdot \frac{1}{\sqrt{\pi}} \cdot (e^{-(D-1)\eta} - (e^{-2h^*})^{\frac{D-1}{2}}) \\
&\geq \frac{\pi^{\frac{D}{2}}}{\Gamma(1 + \frac{D}{2})} \cdot \frac{1}{\sqrt{\pi}} \cdot (e^{-(D-1)\eta} - (1 - (h^*)^2)^{\frac{D-1}{2}}) \\
&= V(\mathcal{B}^D) \cdot \frac{1}{\sqrt{\pi}} (e^{-(D-1)\eta} - (1 - (h^*)^2)^{\frac{D-1}{2}}) \\
&\geq V(\mathcal{B}^D) \cdot \frac{1}{\sqrt{\pi}} (e^{-(D-1)\eta} - 0.2^{\frac{D-1}{2}}),
\end{aligned} \tag{C16}$$

where the last inequality is obtained by  $h^* \geq 0.9$  and  $(1 - (h^*)^2) \leq 0.2$ . Thus, we have proved that:

$$\frac{V(\mathcal{B}_\eta^D)}{V(\mathcal{B}^D)} \geq \frac{1}{\sqrt{\pi}} (e^{-(D-1)\eta} - 0.2^{\frac{D-1}{2}}). \tag{C17}$$

Since  $\eta \leq 0.1$ , the lower bound is larger than 0 when  $D > 1$ , so it is not trivial. Thus, we have proved that

$$\mathbb{P}(\langle \mathbf{a}, \mathbf{b} \rangle \geq \eta) \geq \Omega(e^{-(D-1)\eta} - 0.2^{\frac{D-1}{2}}). \tag{C18}$$

□

**Remark 1.** In Lemma 7, the dimension  $D$  can be interpreted as the degree of freedom of the inner product of two vectors  $\mathbf{a}$  and  $\mathbf{b}$ .

Now, we are ready to prove that quantum gradients for variational LOCC-assisted circuits are free of Barren Plateaus.

Recall Eq. (C3),

$$\frac{\partial \text{Tr} [\hat{H} \Psi_\gamma]}{\partial \gamma_k} = \langle \mathbf{G}^{C_k}, \mathbf{G}^{Q_k} \rangle_F. \tag{C19}$$

With condition  $\mathcal{A3}$  and Lemma 2, the entries in neither  $\mathbf{G}^{C_k}$  nor  $\mathbf{G}^{Q_k}$  are exponentially small as  $n$  scales. We now focus on the inner product structure. The Frobenius inner product of two  $l$ -by- $2^m$  matrices can be interpreted as the inner product of two vectors with length  $l \cdot 2^m$ . However, Lemma 5 indicates that only the entries corresponding to a constant number of non-zero number rows of  $\mathbf{G}^{C_k}$  needs to be considered. Among these rows, Lemma 6 and Lemma 4 indicate that the number of different values in each row is a constant. Thus, the inner product of the two high-dimensional vectors only has a constant degree of freedom  $\mathcal{D}$ ,

$$\mathcal{D} \leq \mathcal{O}(\iota_k \cdot (\max_i(\zeta_i) + \max_j(2^{\nu_j}))) = \mathcal{O}(1) \tag{C20}$$

where  $\zeta_i$ ,  $\nu_k$  and  $\nu_j$  follow the definitions in Lemma 6, Lemma 5, and Lemma 4.

Consequently, with Lemma 7, the probability that  $\frac{\partial \text{Tr}[\hat{H}\Psi_\gamma]}{\partial \gamma_k} \geq \epsilon$  is lower bounded by

$$\mathbb{P}\left(\frac{\partial \text{Tr}[\hat{H}\Psi_\gamma]}{\partial \gamma_k} \geq \epsilon\right) \geq \Omega(e^{-(\mathcal{D}-1)\epsilon} - 0.2^{\frac{\mathcal{D}-1}{2}}) \quad (\text{C21})$$

where  $\mathcal{D} = \mathcal{O}(1)$ , independent of  $n$ . So, the probability  $\mathbb{P}\left(\frac{\partial \text{Tr}[\hat{H}\Psi_\gamma]}{\partial \gamma_k} \geq \epsilon\right)$  is lower bounded by a constant independent of  $n$ . This means that the gradient will not experience exponential decay as  $n$  scales. which completed our proof of the absence of barren plateaus in LOCC-VQE.

## 5. Numerical results for the absence of barren pleatus

We also numerically demonstrate the absence of barren plateaus through the training process of the transverse-Ising model defined in Appendix F 2. Quantum gradient information of the first optimization iteration in LOCC-VQE for the transverse-Ising model is recorded by the mean of the absolute values. The numerical results are shown in Fig. 6.

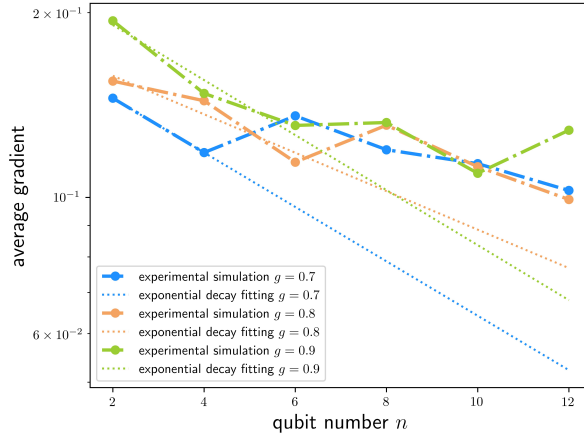


FIG. 6: Average gradients scaling with  $n$ . The mean of the absolute value of the gradients of the first optimization iteration for  $n \in [2, 12]$ . The dot lines represent the exponential decay fitted from the first few average gradient values. The blue, orange, and green curves represent different coupling coefficients  $g = 0.7, 0.8, 0.9$ , respectively.

Notice that under conditions in Theorem 1, the gradients of variational LOCC-assisted circuit do not vanish as the number of qubits  $n$  scales in the asymptotic limit. Due to computational limitations, we can only numerically implement smaller system sizes, where the non-vanishing property of the gradients is less obvious. This is because, from the light cone perspective, the boundaries of the system have a stronger effect on the propagation of information in smaller systems, leading to the decay of the average gradient as shown in Fig. 6. However, even with a small system size, Fig. 6 demonstrates that the quantum gradients for variational LOCC-assisted circuits have a significant separation remain significantly separated from exponentially decaying values under conditions in Theorem 1.

## Appendix D: Quantum mutual information with light cone perspective

### 1. Quantum mutual information

Quantum mutual information is a measure of the correlation between subsystems of the quantum state. It is a quantum mechanical analog of Shannon's mutual information.

Consider a quantum system that can be divided into two non-overlapping subsystems  $A$  and  $B$ . The Hilbert space can be written as the tensor product of two sub-spaces corresponding to the division  $\mathcal{H}_{AB} = \mathcal{H}_A \otimes \mathcal{H}_B$ . For a quantum state  $\rho^{AB}$  defined on the entire Hilbert space  $\mathcal{H}_{AB}$   $\rho^A = \text{Tr}_B(\rho^{AB}) \in \mathcal{H}_A$ , and  $\rho^B = \text{Tr}_A(\rho^{AB}) \in \mathcal{H}_B$  represent the

reduced density matrices of  $\rho^{AB}$  on the two corresponding Hilbert space. Then the quantum mutual information between sub-system  $A$  and  $B$  is defined as:

$$I(A, B) = S(\rho^A) + S(\rho^B) - S(\rho^{AB}), \quad (\text{D1})$$

where  $S(\rho)$  is the von Neumann entropy of the density matrix  $\rho$ :

$$S(\rho) = -\text{Tr}[\rho \log(\rho)]. \quad (\text{D2})$$

Note that the definition of quantum mutual information is naturally extended to two subsystems  $A$  and  $B$  that do not form a partition of the entire quantum system.

## 2. Zero QMI between subsystems with non-overlapping light cones

Here, we prove that if two subsystems  $A$  and  $B$  of the output quantum state of a quantum circuit have non-overlapping information propagation light cones, the quantum mutual information between them is zero.

*Proof.* Let  $\mathcal{L}_A$  be the index set of qubits in the light cone of subsystem  $A$ , and  $\mathcal{L}_B$  be the index set of qubits in the light cone of subsystem  $B$ . Since subsystems  $A$  and  $B$  of the output quantum state of this quantum circuit have non-overlapping light cones, we have

$$\mathcal{L}_A \cap \mathcal{L}_B = \emptyset. \quad (\text{D3})$$

Denote the  $n$ -qubit output state of the circuit as  $\rho$ . Let

$$\begin{aligned} \rho^{\mathcal{L}_A, \mathcal{L}_B} &= \text{Tr}_{[n] \setminus (\mathcal{L}_A \cup \mathcal{L}_B)}(\rho) \\ \rho^{\mathcal{L}_A} &= \text{Tr}_{[n] \setminus \mathcal{L}_A}(\rho) \\ \rho^{\mathcal{L}_B} &= \text{Tr}_{[n] \setminus \mathcal{L}_B}(\rho) \end{aligned} \quad (\text{D4})$$

be the output state tracing out all qubits not in the light cone of  $A$  or  $B$ . Without overlap between the light cones, we can write  $\rho^{\mathcal{L}_A, \mathcal{L}_B}$  in the product form

$$\rho^{\mathcal{L}_A, \mathcal{L}_B} = \rho^{\mathcal{L}_A} \otimes \rho^{\mathcal{L}_B}. \quad (\text{D5})$$

Notice that  $A \in \mathcal{L}_A$ , and  $B \in \mathcal{L}_B$ , we can express subsystem  $A$  and  $B$  of the output state as

$$\rho^{AB} = \rho^A \otimes \rho^B, \quad (\text{D6})$$

where  $\rho^A = \text{Tr}_{[n] \setminus A}(\rho)$ , and  $\rho^B = \text{Tr}_{[n] \setminus B}(\rho)$ . Thus, we have

$$\begin{aligned} I(A, B) &= S(\rho^A) + S(\rho^B) - S(\rho^{AB}) \\ &= S(\rho^A) + S(\rho^B) - S(\rho^A \otimes \rho^B) \\ &= 0. \end{aligned} \quad (\text{D7})$$

□

## Appendix E: Circuit Architectures

### 1. Cartan Decomposition for two-qubit gates

We use the Cartan decomposition of  $SU(4)$  to parameterize the unitary local two-qubit gates in our optimization process, as illustrated in Fig. 7. Similar to [34],  $R_x, R_y, R_z$  are single-qubit rotation gates with generators  $X, Y, Z$ .  $R_{xx}, R_{yy}, R_{zz}$  are two-qubit rotation gates with generators  $X \otimes X, Y \otimes Y, Z \otimes Z$ . Parameterized by  $\theta_x, \theta_y, \theta_z, \theta_{xx}, \theta_{yy}, \theta_{zz} \in [0, 2\pi)$ ,  $R_x(\theta_x)R_y(\theta_y)R_z(\theta_z)$  forms an universal single qubit gate. Together with  $R_{xx}(\theta_{xx})R_{yy}(\theta_{yy})R_{zz}(\theta_{zz})$ , this block can represent a universal two-qubit unitary gate.

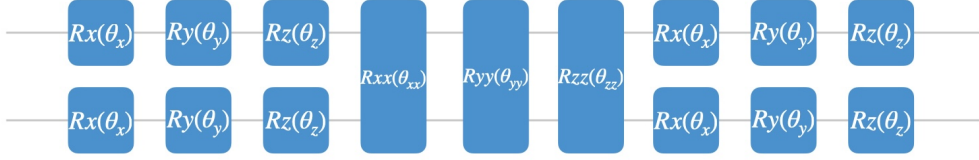


FIG. 7: Cartan decomposition of unitary two-qubit gate.

## 2. Circuit architecture for numerical simulations

To prepare the GHZ state with perturbations and the ground states of the transverse-field Ising model, we adopt a similar architecture for LOCC-VQE. We first apply two layers of local two unitary gates parameterized through Cartan decomposition. Each local two-qubit gate acts on a data qubit and its neighboring ancillary qubit. We then measure all ancillary qubits and feed the measurement outputs into the classical function  $g$ . We set the output of  $g$  to be the parameters of one layer of the single-qubit rotation gate on all data qubits. We empirically set the classical function  $g$  to be the summation of one layer of neural network and neurons linking measurement results from far-apart ancillary qubits to enhance the power of preparing long-range entanglements. The empirical design of  $g$  also shares the idea of the LOCC preparation protocol of the unperturbed GHZ state in [12].

To prepare the ground state of the perturbed rotated surface code, we adopt a similar architecture of error correction. We first applied four layers of parameterized local two-qubit gates through the Cartan decomposition. Each two-qubit gate acts on a data qubit and an associated syndrome qubit following the stabilizer formalism of rotated surface code. Later, all ancillary qubits are measured, and the results are fed into the classical function  $g$ . The output of  $g$  will be set as the parameters of one layer of the single-qubit rotation gate on all data qubits at the end of the quantum circuit.

## 3. Brick wall quantum circuit

For all unitary VQE used in this paper, we adopted the parameterized brick wall quantum circuit as the circuit ansatz, in which all two-qubit gates are parameterized through the Cartan decomposition. The brick wall quantum circuit has a structure as illustrated in Fig. 8. It is formed by consecutive layers of interleaving parameterized local two-qubit gates with a compact layout.

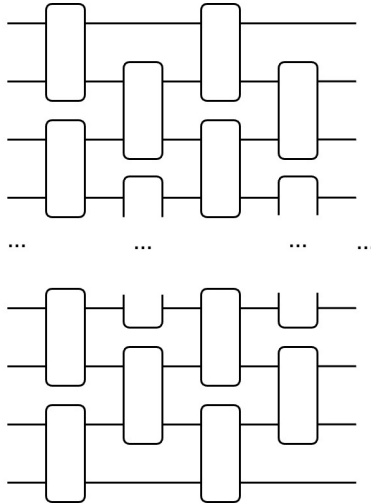


FIG. 8: Brick-wall quantum circuit

#### 4. Training details

The numerical simulation is computationally demanding due to the exponential scaling of the computational time and memory as the qubit number  $n$  scales up. We use the current state-of-the-art tensor-network-based quantum simulation technique [36] combined with an efficient machine learning framework and massive parallelization during the simulation. With efforts combined, we can simulate up to 20 qubits implementing LOCC-VQE.

To save numerical costs, we assume a sufficient number of samplings in most of our numerical simulations. We use block-diagonal unitary two-qubit gates to represent classical control and single-qubit rotations of the data qubits. We also use the sample-based version to prepare the ground state for a smaller system size. In each training iteration, we set the sample round to 100 and used a combination of one layer of neural network as well as empirically set functions to enhance the representability of the classical function. We illustrate the results in Appendix F 4.

Due to numerical costs, we didn't simulate a larger physical system or use more sample rounds in the sample-based simulation. However, since most computation resources are used for parallel sampling and quantum circuit simulation, real quantum experiments would not face this problem. The sampling cost of LOCC-VQE is the same as the unitary VQE protocol as discussed in Section II.

### Appendix F: Additional numerical simulation results

#### 1. Parent Hamiltonian of the Greenberger–Horne–Zeilinger state with perturbations

Besides the Pauli  $X$  perturbation shown in Fig. 3, we also numerically simulate the GHZ state with Pauli  $Y$  and Pauli  $Z$  perturbations. The results are illustrated in Fig. 9

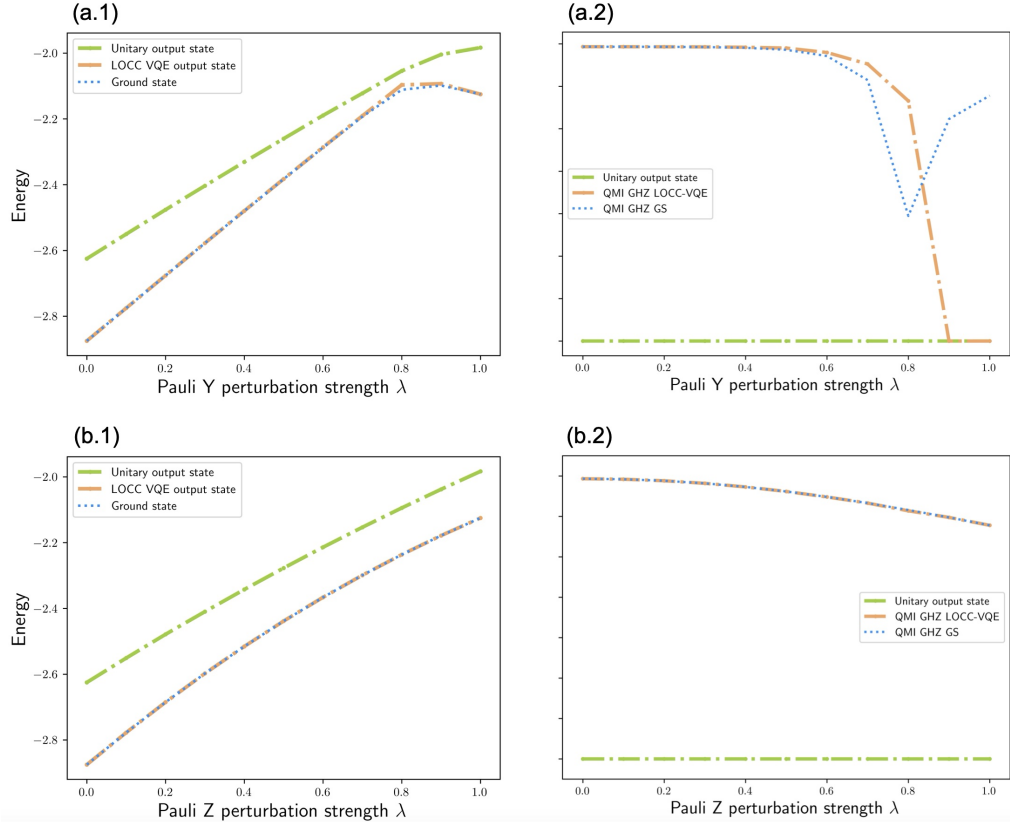


FIG. 9: Numerical simulation results of solving the parent Hamiltonian of the 8-qubit GHZ state with Pauli  $Y$  and  $Z$  perturbations with depth two circuits. (a) Comparison between the energy optimization results through LOCC-VQE and unitary VQE with depth two circuits. (b) Comparison between the quantum mutual information between subsystems  $A$  and  $C$  as shown in Fig. 2 (a).



## 2. Transversed-field Ising model

As another case of the above Hamiltonian in Eq. (5), we also test the 1D transverse-field Ising model,

$$\hat{H}_{\text{tfIsing}} = - \sum_{\langle i,j \rangle} Z_i Z_j - \lambda \sum_j X_j. \quad (\text{F1})$$

The difference is that we do not introduce the degeneracy-breaking term, namely setting  $h = 0$  in Eq. (5). The model exhibits long-range entanglement at its critical point  $|\lambda| = 1$  with a sufficiently large system size.

We numerically compare the energy accuracy of LOCC-VQE in solving a 8-qubit transverse-field Ising model to its unitary counterpart, with results shown in Fig. 10. The result suggests the advantages of LOCC-VQE when  $\lambda$  is near or larger than 1, the phase transition point.

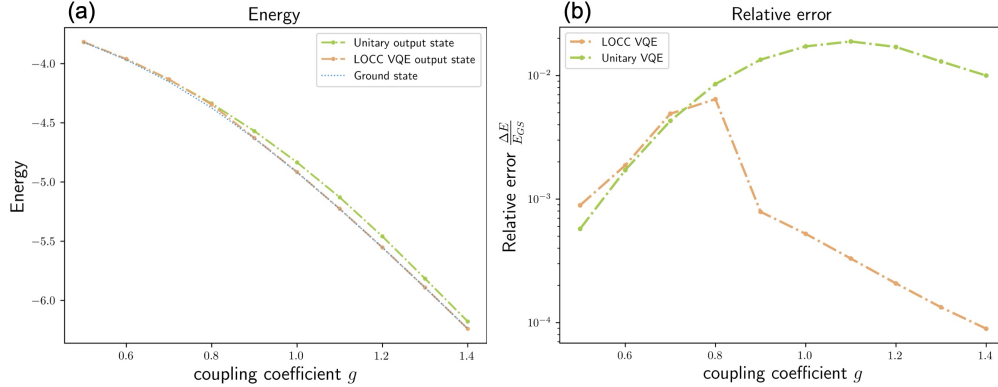


FIG. 10: Numerical simulation results of solving the 8-qubit transverse-field Ising model. (a) Comparison between the energy optimization results through LOCC-VQE and unitary VQE with depth two circuits. (b) Comparison between the relative error of ground state energy optimization results,  $\frac{\Delta E}{E_{GS}} = \frac{E - E_{GS}}{E_{GS}}$ , through LOCC-VQE and unitary VQE with depth two circuits.

The quantum mutual information between sub-regions  $A$  and  $C$ , as illustrated in Fig. 2 (a), is numerically demonstrated for the transverse-field Ising model near the phase transition point, depicted in Fig. 11. The small energy gap between the ground state's subspace and the first excited state subspace when  $g < 1$  makes the optimization process tend to prepare a superposition of the ground state and the first excited state. However, when the  $g$  approaches the quantum phase transition point, the energy gap between the ground state and the first excited state gets larger, and LOCC-VQE can accurately capture the long-range entanglement of the ground state of the transverse-field Ising model.

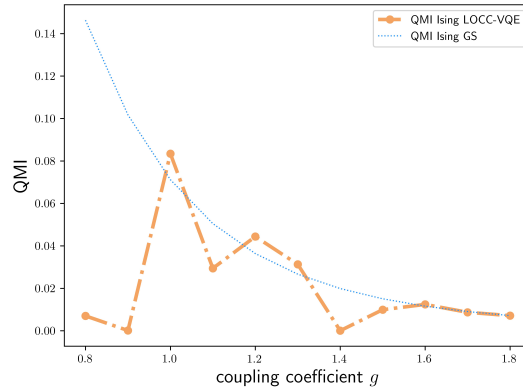


FIG. 11: QMI of sub-region  $A$  and  $C$  for transverse-field Ising model. The blue dot line represents the theoretical QMI of a state in the ground state subspace of the transverse-field Ising model's Hamiltonian. The orange dot-slash line represents the QMI of the state prepared by LOCC-VQE.

### 3. Toric code

The toric code is a quantum error-correcting code defined on a two-dimensional rectangular lattice with periodic boundary conditions. The ground states of the toric code Hamiltonian possess long-range entanglement, enabling the storage of logical information.

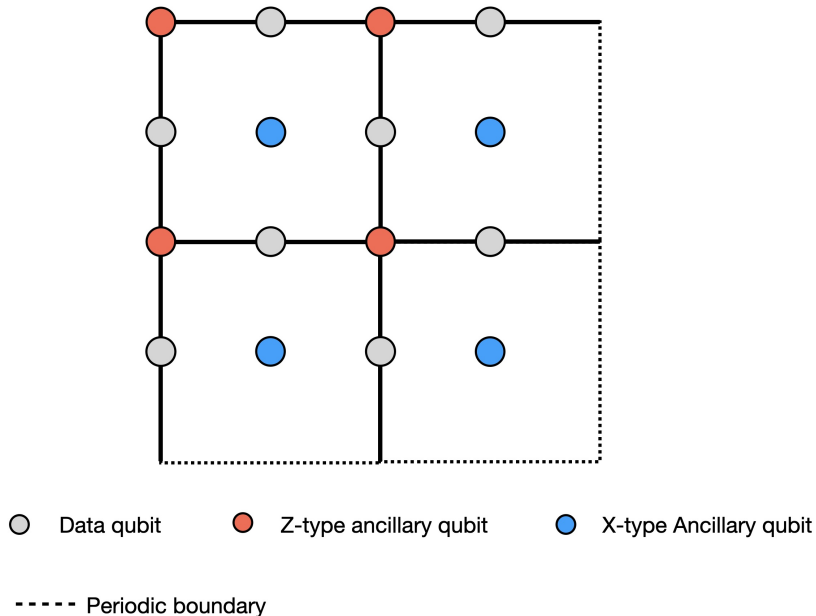


FIG. 12: Two-dimensional toric code’s lattice. An edge represents a data qubit, a vertex represents a Z-type ancillary qubit corresponding to a Z-stabilizer, and a plaquette represents an X-type ancillary qubit corresponding to an X-stabilizer. The dotted lines on the boundary represent periodic boundary conditions, i.e., the left-most and the right-most edges are equivalent, and the upper-most and the lower-most edges are equivalent.

In our numerical tests, we add a magnetic field in the  $Z$  direction as a perturbation, resulting in the following Hamiltonian

$$\hat{H}_{\text{tor}}(\lambda) = -(1 - \lambda) \sum_v A_v - (1 - \lambda) \sum_p B_p - \lambda \sum_{i=1}^{N_x N_y} P_i, \quad (\text{F2})$$

where  $N_x$  and  $N_y$  are width and height of the regular lattice,  $A_v$  and  $B_p$  are stabilizers for the unperturbed rotated surface code, and  $\lambda$  is the perturbation strength and  $P_i \in X_i, Y_i, Z_i$  on the  $i$ -th site. The Z-type stabilizers  $A_v$  and X-type stabilizers  $B_p$  correspond to vertices and plaques on the lattice respectively, illustrated in Fig. 12.

The numerical results are illustrated in Fig. 13. We can achieve  $10^{-2}$  accuracy in relative error among all perturbation strengths.

We also compared the results of LOCC-VQE with the result of measurement-based variational quantum eigensolver [31] over the same perturbed toric code model. LOCC-VQE can achieve higher accuracy than MB-VQE, as illustrated in Table I.

TABLE I: Comparison between the relative error of preparing the ground states of perturbed toric code by LOCC-VQE and MB-VQE.

$\max_{\lambda} \left( \frac{\Delta E}{E_{GS}} \right)^a$	Pauli $Y$ perturbation	Pauli $Z(X)$ perturbation
LOCC-VQE	0.0735	0.0234
MB-VQE [31]	<sup>b</sup>	0.0378

<sup>a</sup> The form of perturbation used in MB-VQE is slightly different from the form in Eq. (F2). However, we can still compare the results by calculating the relative error.

<sup>b</sup> Pauli  $Y$  perturbation is not demonstrated in this reference.

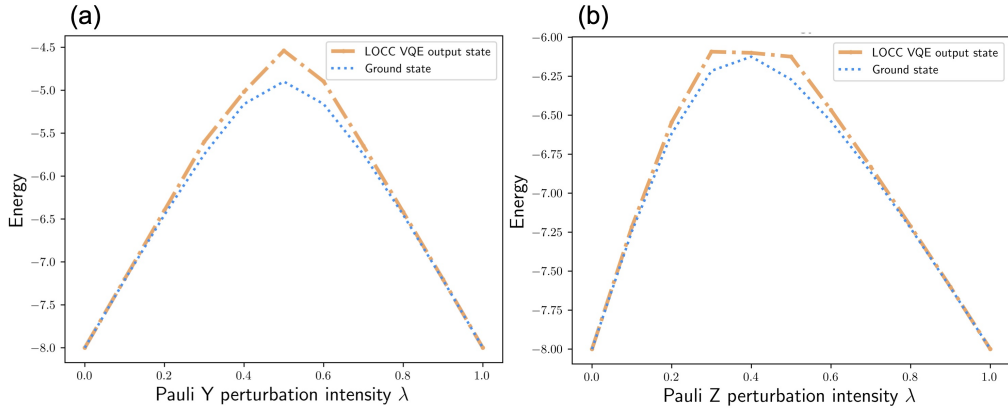


FIG. 13: Numerical simulation results of the toric code with Pauli  $Y$  (a) perturbation and Pauli  $X$  ( $Z$ ) (b) perturbation. Due to symmetry, Pauli  $X$  perturbation is equivalent to Pauli  $Z$  perturbation up to a change of basis.

#### 4. Sampling-based numerical simulations

We numerically simulate the sampling process during mid-circuit measurements, and we call it sampling-based LOCC-VQE in our numerical simulations. The results of using sampling-based LOCC-VQE for the 4-qubit GHZ states with perturbations are shown in Fig. 14, and the results for transverse-field Ising model are depicted in Fig. 15. As shown in the numerical results, the states prepared by LOCC-VQE have ground state energy accuracy, even with the presence of sample inaccuracy and much smaller optimization iterations.

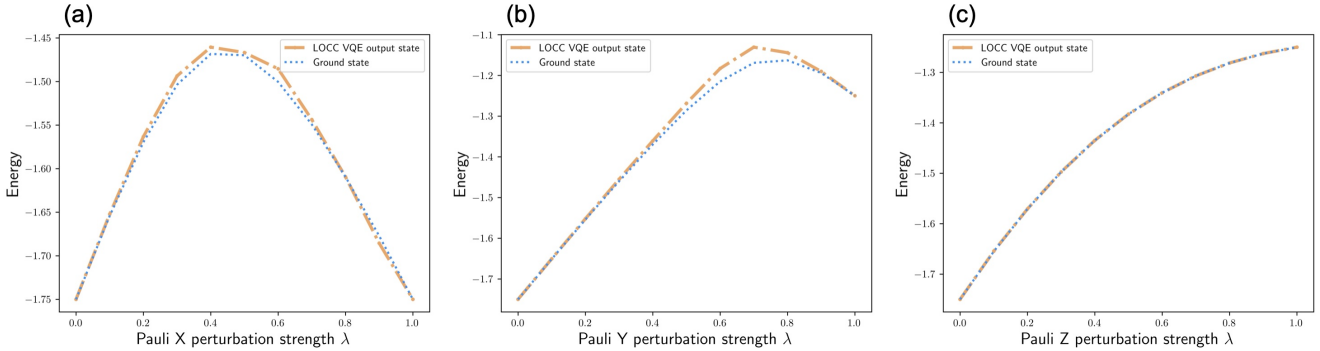


FIG. 14: Numerical simulation results of solving the parent Hamiltonian of the four-qubit GHZ state with Pauli  $X$  (a),  $Y$  (b), and  $Z$  (c) perturbations. The results are achieved through sample-based LOCC-VQE.

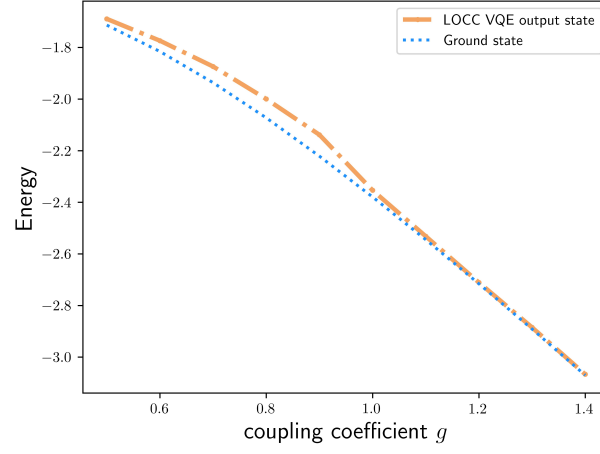


FIG. 15: Numerical simulation results of solving transverse-field Ising model with four qubits with sample-based LOCC-VQE.